



## Global motion reconstruction of a steel catenary riser under vessel motion

Jungao Wang, Shixiao Fu, Rolf Baarholm, Mengmeng Zhang & Chang Liu

To cite this article: Jungao Wang, Shixiao Fu, Rolf Baarholm, Mengmeng Zhang & Chang Liu (2019) Global motion reconstruction of a steel catenary riser under vessel motion, Ships and Offshore Structures, 14:5, 442-456, DOI: [10.1080/17445302.2018.1500785](https://doi.org/10.1080/17445302.2018.1500785)

To link to this article: <https://doi.org/10.1080/17445302.2018.1500785>



Published online: 25 Jul 2018.



Submit your article to this journal [↗](#)



Article views: 319



View related articles [↗](#)



View Crossmark data [↗](#)



Citing articles: 2 View citing articles [↗](#)



# Global motion reconstruction of a steel catenary riser under vessel motion

Jungao Wang<sup>a,b,c</sup>, Shixiao Fu<sup>a,b,d</sup>, Rolf Baarholm<sup>e</sup>, Mengmeng Zhang<sup>a,b</sup> and Chang Liu<sup>a,b</sup>

<sup>a</sup>State Key Laboratory of Ocean Engineering, Shanghai Jiao Tong University, Shanghai, People's Republic of China; <sup>b</sup>Collaborative Innovation Center for Advanced Ship and Deep-Sea Exploration, Shanghai Jiao Tong University, Shanghai, People's Republic of China; <sup>c</sup>Department of Mechanical and Structural Engineering and Materials Science, University of Stavanger, Stavanger, Norway; <sup>d</sup>SINTEF Ocean, Trondheim, Norway; <sup>e</sup>Statoil, Trondheim, Norway

## ABSTRACT

Under vessel motion, dynamic responses of compliant risers, like a steel catenary riser, are no longer small displacement and small deformation problems but characterised with large displacement and small deformation instead. It is therefore difficult to directly obtain the riser global motion based on experimental or field-measured local strain or acceleration data. This paper proposes a generalised global motion reconstruction method for large displacement but small deformation problems, assuming that the global motion can be divided into quasi-static motion and dynamic vibration. The proposed methodology is validated numerically and experimentally with satisfactory accuracy. Parameters like sensor location and mode number to be used in the motion reconstruction are optimised and recommended. Uncertainty analysis considering different noise levels is performed to evaluate the robustness of the proposed method. Most importantly, further comparative hydrodynamic analyses indicate the significance of the drag amplification effect, most probably due to vortex-induced vibrations.

## ARTICLE HISTORY

Received 3 December 2017  
Accepted 19 June 2018

## KEYWORDS

Motion reconstruction; riser global motion; vessel motion; uncertainty analysis; hydrodynamic coefficient identification

## Nomenclature

|                      |  |
|----------------------|--|
| $R$                  | Radius of the riser ( $m$ )  |
| $s$                  | Axial length ( $m$ )   |
| $T$                  | Tension  |
| $EI$                 | Bending stiffness ( $N \cdot m^2$ )  |
| $EA$                 | Tensile stiffness ( $N$ )  |
| $\phi$               | Riser inclination angle with respect to the horizontal plane ( $^\circ$ )                    |
| $\rho$               | Density of water ( $kg/m^3$ )  |
| $g$                  | Gravity acceleration ( $m/s^2$ )   |
| $x, y, z$            | Riser global coordinate, in-plane horizontal, out-of-plane horizontal and vertical direction |
| $A$                  | Riser cross section area ( $m^2$ )   |
| $A_n$                | Displacement component normal to the riser axis ( $m$ )                                      |
| $V_n$                | Velocity component normal to the riser axis ( $m/s$ )  |
| $A_{orca}, V_{orca}$ | Calculated displacement and velocity amplitudes by Orcaflex ( $m, m/s$ )                     |
| $A_{re}, V_{re}$     | Reconstructed displacement and velocity amplitudes ( $m, m/s$ )                              |
| $y_{in-n}$           | In-plane displacement normal to the riser axis ( $m$ )                                       |
| $p$                  | Modal weight of displacement   |
| $\varphi$            | Modal shape of the displacement  |
| $\kappa$             | Curvature ( $1/m$ )  |
| $\varepsilon$        | Strain   |
| $l_s, l_e$           | Starting and ending length of the riser segment for mode superstitution ( $m$ )              |
| $m, n$               | Mode number  |
| $\xi$                | Error  |
| $\Delta$             | Noise level  |
| $A_{im}$             | Scaled top imposed motion amplitude at real hang-off point ( $m$ )                           |
| $T_{im}$             | Scaled top imposed motion period at real hang-off point ( $s$ )                              |
| $KC$                 | $KC$ number  |
| $C_D$                | Drag coefficient   |

## 1. Introduction

As oil and natural gas exploration and production extend to increasingly deep waters, the cost of the riser systems and technological challenges increase rapidly. The use of compliant risers such as steel catenary riser (SCR) and steel lazy wave riser (SLWR) are potential solutions for deep-water oil and gas production systems (DNV 2010). A SCR is a prolongation of a sub-sea pipeline attached to a floating production structure in a catenary configuration. The first SCR was installed by Shell in the Auger tension leg platform (TLP) in 1994 at a water depth of 872 m (Mekha 2001).

In the designing point of view, fatigue damage is one of the major concerns for the SCR lines, due to the vessel motion, the wave and the current. As addressed in DNV-OS-F201 (DNV 2001), three different contributions to the fatigue damage should be considered: the wave-induced, the vessel motion-induced- and the vortex-induced stress cycles.

Wave-induced stress cycles are caused by the direct wave loading on the riser. Due to the rapid decay effect of the deep-water wave with the increasing water depth (Faltinsen 1993), the fatigue damage caused by the wave-induced stress cycles mainly locates at the uppermost of the riser and therefore has limited influence on the entire riser. As to the vessel motion effect, the entire riser will move back and forth in the water considering a top moving boundary condition, and therefore leads to significant stress cycles and fatigue damage to the riser. When the riser is exposed to the ocean current, vortices are generated in the wake of the riser. Vortex-induced vibration (VIV) happens to the marine slender structures when the

vortex shedding frequency approaches one or several of the structural natural frequencies (Vandiver and Li 2005). The alternate vortex shedding would lead to oscillating cross-flow (CF) and in-line (IL) forces, which causes the riser to vibrate perpendicularly and in-line to the ambient flow. Such periodic bending stress cycles from VIV may lead to rapid accumulation of fatigue damage of the riser systems (DNV 2005). VIV is also known to amplify the drag force partly due to a larger projected cross section under the cross-flow vibration (Vandiver and Li 2005). VIV is associated with both the in-line drag force and cross-flow lift force. It should be mentioned that the hydrodynamic loads of the riser subjected to wave, vessel motion and VIV can all be described by the Morrison Equation type of expressions (one part in phase with the structure velocity and the other part in phase with the acceleration).

Generally speaking, the riser dynamic stresses (responses) under wave and vessel motion can be calculated synchronously in time-domain in the state of the art riser design and analysis software (Orcina 2012). We may call this the riser global analysis, where the vessel motion is treated as a moving boundary problem, and the hydrodynamic loads (expressed as Morrison forces) are considered using the relative velocity between the structure and the water particles. The water particle motion under wave, current and riser's own motion are all considered to determine the relative velocity. The hydrodynamic coefficients need to be carefully chosen in order to achieve reasonable results. To the Morrison Equation in the global analysis, the force coefficients are the drag and added mass coefficients, which are considered to be dependent on the Reynolds number, Keulegan-Carpenter (KC) number and surface roughness according to experimental observations (Sumer 2006). The hydrodynamic coefficients should be determined beforehand and are assumed to be unchanged during the entire simulation. As to the riser VIV under ocean current, it is a non-linear, self-regulated and multi-degree-of-freedom phenomenon and involves strong fluid-structure interactions. The hydrodynamic coefficients associated with VIV are excitation and added mass coefficients, which are functions of VIV response frequency, amplitude and they are also sensitive to the Reynolds number and surface roughness. Typically, the added mass coefficient is determined beforehand and the excitation coefficient is found through iteration assuming VIV under ocean current is a dynamic energy balance process (Vandiver and Li 2005). With certain assumptions, the riser global responses under vessel motion and VIV responses under ocean current can be solved separately by frequency- or time-domain finite element method. Considering the significant in-plane drag amplification caused by out-of-plane VIV, a rerun of global analysis using amplified drag coefficient is recommended to get better results (Larsen et al. 2001). Ideally, they should be a coupled problem and to be solved simultaneously. However, due to the complexities of VIV, it's hard to find a robust time-domain prediction algorithm.

It's worth noting that recent research results reveal that VIV will also occur at the sag-bend of a SCR or other highly compliant rigid (HCR) risers due to the vessel motion such as heave (Grant et al. 1999). This phenomenon occurs because

the riser will be exposed to the oscillatory flow field due to its motions in still water, even without the existence of ocean current. Once the shedding frequency under oscillatory flow approximates the riser natural frequency, the riser will further experience intermittent out-of-plane vibration, known as vessel motion-induced VIV (Wang, Fu and Baarholm 2014, Wang et al. 2015). Such vessel motion-induced VIV is also found to have caused substantial fatigue damage to the riser system (Wang, Fu, Baarholm, et al. 2014). This phenomenon indicates that the coupling effect between the riser global and VIV responses are far more complicated than we expect. The hydrodynamic load distribution for a large aspect ratio riser in the real case scenario is, therefore, quite different from those estimated using the empirical force coefficient (from rigid cylinder test (Gopalkrishnan 1993)) and strip theory where the real flow field (characterised with high Reynolds number), riser span-wise coupling and global-VIV response coupling are all missed. Therefore, discrepancies between the numerical predictions and the model test or the field measurements are always expected and observed. The root cause of these discrepancies is the inadequate understanding on the real hydrodynamic force distribution. An alternative way to bridge such gap is to directly investigate the hydrodynamic load distribution of the risers during the model test or the field measurements.

There have been emerging researchers working on the hydrodynamic load distribution for the risers undergoing VIV based on the inversed analysis techniques (Wu 2011, Song et al. 2016). The inversed analysis is defined against the traditional structural dynamic analysis where the loads are known, and the responses are to be calculated. The procedure of an inversed analysis, on the other hand, needs to know the structural responses including the displacement, velocity and acceleration beforehand. Finite Element Method (FEM) is then used to construct the entire riser system kinematics equation and to further obtain the load distribution. To the authors' knowledge, the published literatures all deal with the model test cases where the riser model is a constraint at both ends (either pinned or fixed). In this case, the riser VIV response is a small displacement, small deformation problem, where the response (displacement, velocity and acceleration) can be reconstructed using the modal superposition method. However, in reality, most of the risers are attached to a floating structure which is in fact a moving boundary to the risers. The riser (especially the compliant risers, like a SCR) response is no longer the small deformation problem but characterised with large displacement but small deformation instead.

This paper proposes a generalised global motion reconstruction method for the marine slender structures characterised with large displacement but small deformation. The proposed methodology is validated numerically and experimentally with uncertainty analysis. Meanwhile, parameters like sensor location and mode number to be used in the motion reconstruction are also optimised and recommended. Comparison of the reconstructed motion results considering measurements with different artificial noise level indicates a strong robustness of the proposed method. Further hydrodynamic coefficients analysis suggests an obvious drag amplification by VIV.

The proposed motion reconstruction methodology successfully captures the riser in-plane global motion under vessel motion, which provides essential inputs for the future research on accurate hydrodynamic load distribution.

## 2. Problem statement

In this paper, we focus on the motion reconstruction for a SCR under vessel motion. The sketch of a SCR is shown in Figure 1, where it is firstly connected to the well head, followed by a certain length of riser laying on the sea floor, known as the flow-line region. The SCR then starts to incline increasingly from the touch down point (TDP) to the hang-off point at the floating vessel, forming a catenary configuration in the middle, known as the sag-bend region.

In the real sea state, the floating vessel will move in six degrees of freedom. The connecting riser will also have considerable global motion back and forth in the water. Meanwhile, the TDP location will vary as well due to the vessel motion. Generally speaking, the riser global motion is characterised with low frequency, large displacement and small deformation. The catenary geometry and TDP variation further introduce the non-linearity into the whole riser response.

As has been described in the introduction that this riser global motion will not only lead to fatigue damage, but also induce VIV in the transverse direction. The existence of transverse VIV will in turn affect the hydrodynamic load distribution along the riser, and therefore alter the global motion. Accordingly, to obtain the accurate riser global motion would help the understanding of the hydrodynamic load distribution, and vice versa. In this paper, we try to propose a method which is capable of reconstructing the accurate riser global motion in time-domain based on the experimental or field measurements (bending strain and vessel motion time histories). This method will be verified both numerically and experimentally.

## 3. Motion reconstruction method

As has been introduced about the complicity of the riser global motion under vessel motion, it is, however, believed that the riser global motion can be simplified under certain assumptions. In this paper, we take the riser in-plane motion as an

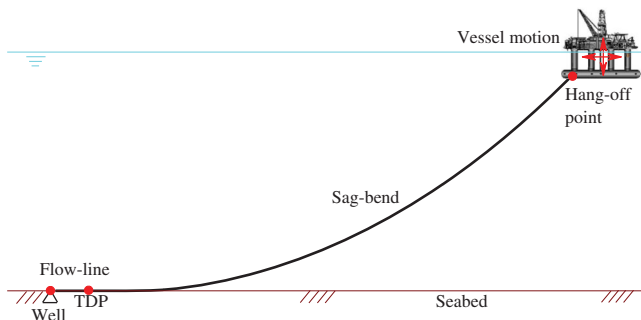


Figure 1. Sketch of a steel catenary riser connected to a floating platform. This figure is available in colour online.

example for demonstration. More complicated three-dimensional motion should be applicable by adding an out-of-plane orthogonal dimension.

As illustrated in Figure 2, when the vessel starts to move from location A to location B, the riser global motion can be divided into two individual components:

- (1) The quasi-static motion from one static configuration (black solid line) to another static configuration (green dashed line). This quasi-static motion is only due to the riser upper boundary condition variation from location A to location B;
- (2) The dynamic vibration, as illustrated by the blue dot-dashed line and the red dot line, which superimposed on the static configurations.

The following riser global motion reconstruction methodology is based on the above assumption.

### 3.1. Quasi-static motion reconstruction

As has been mentioned that the quasi-static motion is in fact the SCR static configuration variation under different vessel locations, therefore, this quasi-static part of the motion reconstruction can be achieved by solving the SCR static equation at each time step.

As shown in Figure 3, a sketch of the SCR is presented. The global coordinate  $x$ - $z$  is established, where the point right above the static TDP on the mean water level is set to be the origin of coordinate.  $s$  in Figure 3 denotes the instant axial length of the riser,  $\phi$  is the riser inclination angle with respect to the horizontal plane, and  $T$  is the axial tension.  $T_H$  and  $T_w$  are the tension at the TDP and the top hang-off point, respectively. To a SCR, the horizontal component of the axial tension is the same along the whole riser.

Meanwhile, a detailed force analysis diagram on a finite SCR segment with the axial length of  $ds$  is also illustrated in Figure 3. There are mainly five force counterparts, two tension components at both ends:  $T$  and  $T + dT$ , two buoyancy compensation components:  $-\rho g z A$  and  $-\rho g(z + dz)A$ , and the wet weight component. If we write the equilibrium equations

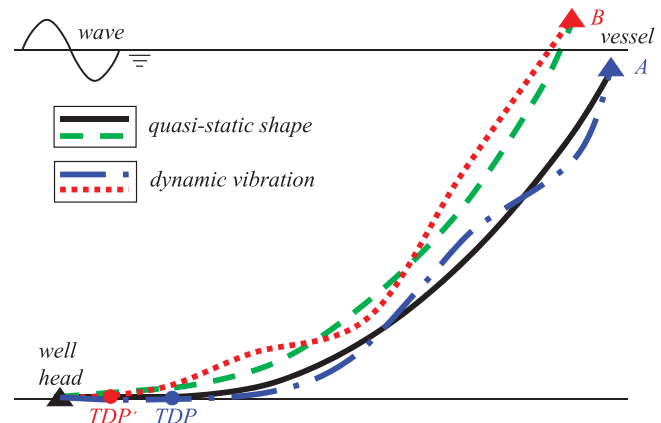
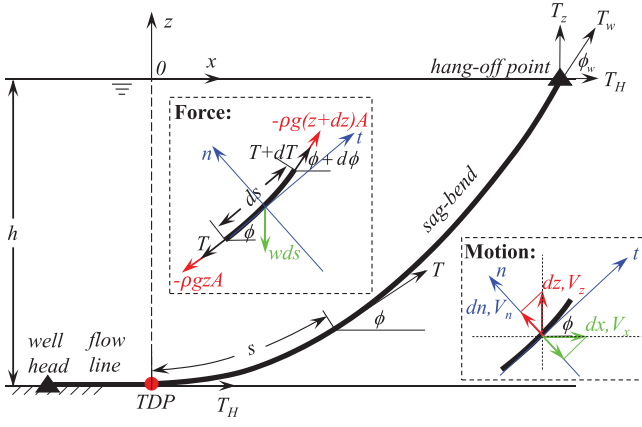


Figure 2. Sketch of a dynamic steel catenary riser under vessel motion. This figure is available in colour online.



**Figure 3.** Sketch of a SCR under static equilibrium state and the segment force equilibrium diagram. This figure is available in colour online.

along the tangential and normal directions for this segment, we can get:

$$\text{Normal direction: } dT - \rho g A dz = w ds \cdot \sin \phi \quad (1)$$

$$\text{Tangential direction: } T d\phi - \rho g A dz = w ds \cos \phi \quad (2)$$

By combining the Equations (1) and (2), and further integrate these force relationships along the whole sag-bend length, we can have the general catenary equation as:

$$\begin{aligned} z(s) &= \frac{T_H}{w} \left( \cosh \frac{x(s)}{(T_H/w)} - 1 \right) - h \\ x(s) &= \frac{T_H}{w} \ln \frac{1 + \sin \phi(s)}{\cos \phi(s)} \\ s(s) &= \frac{T_H}{w} \sinh \left( \frac{x(s)}{(T_H/w)} \right) \\ T'(s) &= T_H + w(z(s) + h) \\ \varepsilon_{\text{quasi}}(s) &= \frac{\frac{d^2 z(s)}{dx(s)^2}}{\left( 1 + \left( \frac{dz(s)}{dx(s)} \right)^2 \right)^{\frac{3}{2}}} R \end{aligned} \quad (3)$$

where  $T' = T - \rho g z A$ ,  $\varepsilon_{\text{quasi}}$  is the bending strain caused due to the SCR geometry.

The normal component of the riser motion can be expressed by

$$\begin{aligned} dn(s) &= dz(s) \cdot \cos \phi(s) - dx(s) \cdot \sin \phi(s) \\ V_n(s) &= Vz(s) \cdot \cos \phi(s) - Vx(s) \cdot \sin \phi(s) \end{aligned} \quad (4)$$

where  $dn$ ,  $V_n$  are the displacement and velocity components that normal to the riser axis, while  $dx$ ,  $V_x$  and  $dz$ ,  $V_z$  are the horizontal and vertical components, respectively, and  $\phi$  is the local riser inclination angle with respect to the horizontal plane. This motion relationship is also illustrated in Figure 3.

Typically, the known variables are the total length of the riser, the horizontal and vertical length from the wellhead to the vessel location, and the cross-section properties of the

riser. By solving the catenary equation for any giving vessel location, the static configuration of the SCR can be well defined. The quasi-static motion is then constructed by differentiate the static configurations of the two continuous time steps.

It should be mentioned that the TDP would move back and forth as the vessel changes its position, this is a non-linear feature which can be partly captured in the quasi-static motion reconstruction stage.

### 3.2. Dynamic vibration reconstruction

The dynamic vibration can be reconstructed based on the linear mode superposition, where the vibration displacement can be expressed as a sum of mode shapes with different modal weights at any time step:

$$y_{in,n}(t, s) = \sum_{i=m}^n p_i(t) \varphi_i(s), \quad s \in [l_s, l_e] \quad (5)$$

where  $y_{in,n}(t, s)$  is the reconstructed vibration displacement in time history along the riser length, and the displacement here is in the normal direction with respect to the riser axis in the SCR plane.  $p_i(t)$  is the  $i$ th modal weight of displacement, and  $\varphi_i(s)$  is the  $i$ th mode-shape of the displacement.  $l_s$ ,  $l_e$  is the starting and ending length of the riser segment for mode superposition. It should be mentioned that since the dynamic vibration is reconstructed based on the linear mode superposition from mode number  $m$  ( $m \geq 1$ ) to mode number  $n$ , the non-linear effect of the TDP variation cannot be captured in this part.

The mode shapes we use in the dynamic vibration reconstruction are calculated based on the static SCR configuration when there are no dynamic loads. Three representative in-plane mode shapes are illustrated in Figure 4. The mode shapes are the components that normal to the riser axis, by employing Equation (4).

Based on the small deformation assumption, the curvature  $\kappa(t, s)$  can be expressed by:

$$\kappa(t, s) = \frac{d^2 y_{in,n}}{ds^2} = \sum_{i=m}^n p_i(t) \varphi_i''(s) \quad (6)$$

where  $\varphi_i''(s)$  is the  $i$ th mode-shape of the curvature.

According to the geometric relationship between bending strain and curvature, we have

$$\kappa(t, s) = \frac{\varepsilon(t, s)}{R} \quad (7)$$

where  $R$  is the outer radius of the strain measurement location on the model,  $\varepsilon(t, s)$  is the dynamic strain time histories caused by the dynamic vibration. It should be mentioned that the quasi-static motion would also lead to the curvature and strain variation, as shown in Equation (3). These time-varying components of the quasi-static strain should be eliminated from the total dynamic strain to get the pure dynamic strain for vibration reconstruction.

By combining Equations (6) and (7), the SCR in-plane dynamic vibration can be reconstructed from Equation (5).



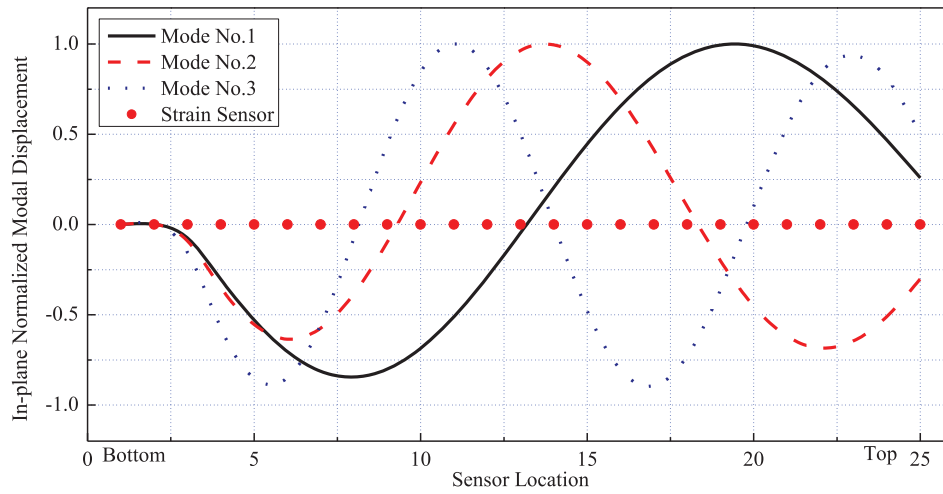


**Figure 4.** In-plane displacement mode shapes of the SCR. This figure is available in colour online.

Finally, by superimposing the quasi-static motion and dynamic vibration, the riser global motion in the normal direction can be reconstructed. It should be mentioned that we are demonstrating the modal superposition using strain information. But the method is also applicable to reconstruct the dynamic vibration if the measurements are the lateral accelerations. In that case, we need to differentiate Equation (5) twice with time in order to link with acceleration.

In order to validate the proposed motion reconstruction method, a numerical model is built for riser global dynamic analysis in Orcaflex (Orcina 2012), after which the riser dynamic displacement, bending strain and vessel motion time histories are all calculated. The above-mentioned motion reconstruction method is then employed to obtain the riser global motion, which is further compared with the directly calculated riser global motion from the numerical simulation. Meanwhile, a large-scale SCR model test is carried out. The motion reconstruction method is employed again to obtain the riser global motion using experimental measurements. The reconstructed motion is further validated against the underwater video measurement at one location in the middle part of the SCR sag-bend. The validation process is illustrated in the below chart:

#### 4. Experimental and numerical model description

The model test was carried out in the ocean basin at Shanghai Jiao Tong University. The end goal of the model test is to investigate the VIV effects and its fatigue damage contribution on SCR under current or top vessel motion (Wang, Fu, Baarholm, Wu and Larsen 2014, Wang, Fu, Baarholm, Wu and Larsen 2015, Wang et al. 2017). While in this paper, part of the experimental data is used to verify the feasibility and accuracy of the proposed motion reconstruction method.

##### 4.1. Experimental description

The test riser is truncated from a 4010 m long production SCR, the key parameters for the full-length SCR, truncated SCR and the scaled SCR are listed in Table 1.

Figure 6 shows the geometrical sketch of the test riser model. The top end of the riser is attached to a two-degree of freedom oscillator with a pinned connection, and the vessel motion is simulated by oscillating the top end of the SCR at given motion trajectories in the riser plane (no out-of-plane vessel motion is considered in this paper). The other end of the model is pinned connected to a sub-fake bottom with the TDP marked in Figure 6. Detailed description about the model test can be found in the published literature (Wang, Fu, Baarholm, Wu and Larsen 2015, Wang, Fu, Larsen, Baarholm, Wu and Lie 2017).

During the model test, top and bottom axial tension are measured using force transducers installed between ends of the model and the motion track systems. In addition, 25 evenly distributed measuring stations, as marked in Figure 6, are chosen to instrument the fibre Bragg grating (FBG) strain sensors for recording the structural dynamic responses. More specifically, sensors are divided into four groups, two for the in-plane and another two for the out-of-plane responses. Motion trajectories of the forced vessel motion are recorded by encoders. All the measurements are sampled synchronously with the sampling frequency at 250 Hz.

There are also several underwater cameras installed in order to capture the global motion of the riser. One specific high-resolution underwater camera is reserved to measure the riser in-plane global motion, corresponding to the location for sensor location 13. The recording rates for the underwater cameras are 25 frames per second.

**Table 1.** Physical properties of the considered SCR.

| Item                                     | Full scale<br>(full length) | Full scale<br>(truncated) | Model scale<br>(measured) |
|--|-----------------------------|---------------------------|---------------------------|
| Total length (m)                         | 4010                        | 456.53                    | 23.71                     |
| Water depth (m)                          | 1500                        | 171.43                    | 9                         |
| Hang-off angle (°)                       | 75                          | 46.24                     | 46.24                     |
| Length of sag-bend (m)                   | 1809.12                     | 401.53                    | 21.0806                   |
| Horizontal length of flow line (m)       | 2200.88                     | 55                        | 2.626                     |
| Horizontal Length of sag-bend (m)        | 886.30                      | 350.81                    | 18.4175                   |
| Outer diameter (m)                       | 0.4                         | 0.4                       | 0.024                     |
| Mass in air (Kg/m)                       | 234.49                      | 234.49                    | 0.69                      |
| Mass ratio                               | 1.82                        | 1.82                      | 1.53                      |
| Bending stiffness $EI$ ( $N \cdot m^2$ ) | $4 \times 10^7$             | $4 \times 10^7$           | 10.5                      |
| Tensile stiffness $EA$ (N)               | $4.14 \times 10^9$          | $4.14 \times 10^9$        | $6.67 \times 10^5$        |

## 4.2. Numerical model description

A numerical SCR model is built in Orcaflex for dynamic analysis considering the top vessel motion, trying to replicate the experimental test cases. The numerical riser model consists of around 1300 line elements, with the same general cross-sectional properties as measured for the test SCR model in Table 1. The boundary conditions of the riser are pinned at both ends for two bending directions, which simulates the universal joints used in the model test. In the dynamic response simulation, the external excitation is the forced motion at the top end of the riser (truncated model), by considering pure harmonic heave motion for the full-length SCR. Therefore, the predefined planar motion at the top end of the SCR consists of the primary vertical component and the secondary horizontal component. The hydrodynamic load on the riser is modelled by the Morrison type of equation, including the added mass force and damping force. It should be mentioned that the drag coefficient is set to be 1.2 and the added mass coefficient is set to be 1.0 for the numerical cases for the purpose of motion reconstruction method validation. It is expected that the real drag and added mass coefficients in the real model tests are quite complex and are different from the above values, partly due to the existence of VIV. Therefore, other cases using alternative hydrodynamic coefficients are also performed and compared with the measured riser responses, in order to find out the most proximate hydrodynamic load coefficients. This part will be discussed in the results and discussions.

In the numerical analysis, the time step is set to be 0.01 s, and the simulation time is 30 times of the vessel motion period. The riser dynamic results are evaluated excluding the transient state at the initial stage of the dynamic analysis.

## 5. Results and discussions

In the following sections, the motion reconstruction method is validated both numerically and experimentally by following the

procedure in Figure 5. The validation is performed based on three representative test cases when the vessel motion is small, medium and large, respectively, as shown in Table 2. While detailed discussion is specified only for the case with medium vessel motion. It should be mentioned that the parameters  $A_i$  and  $T_i$  listed in Table 2 are the prototyped pure harmonic heave motion of the vessel acting on the full-length SCR, while  $A_{im}$  and  $T_{im}$  are the scaled heave motion at the top end of the riser before truncation. The real top end planar motion of the test riser will have both vertical (primary) and horizontal (secondary) components, which simulates the motion trajectories at the truncation point.

In the numerical validation, we compare the riser global motion displacement and velocity, in both peak values and time histories, between the reconstructed and the directly calculated values. The effects from the sensor location, mode numbers used in the reconstruction are discussed and also the tolerance on different noise level of the measurements are evaluated.

### 5.1. Numerical validation results

#### 5.1.1. Sensor location effect

As has been mentioned in Figure 6 that there are 25 sensor locations along the axial direction, among which the first two locations are in the flow-line section. Due to the vessel motion, part of the flow line will be lifted and dropped periodically, which further causes the TDP variation. It is expected that this phenomenon cannot be captured by the linear mode superposition we proposed for dynamic vibration reconstruction. This is because the inputs we have for the dynamic vibration reconstruction are the strain time histories and the mode shapes. The strain time histories will be strongly non-linear at the measuring stations around the TDP region due to the TDP variation. Therefore, introducing the measurements (non-linear strain) in the flow line and near the static TDP would potentially bring errors and uncertainties into the linear modal superposition (the matrices algorithm in Equations (5)–(7)).

However, it is important for us to understand the effects of the number of sensor locations used for motion reconstruction, in order to have the best approximation against the real riser motion. Figure 7 presents the comparison on the in-plane normal displacement amplitude among the conditions using different sensor location combinations for the case H\_A021T481. It is obvious that the reconstructed motions by introducing the strain information in the flow line (indicated by the red circles) and also the location near the static TDP (sensor location 3, indicated by the navy triangles) have a notable deviation from the real motion calculated by Orcaflex (indicated by the black squares). While the other two results using information from sensor location 4 (indicated by the green pentagons) and location 5 (indicated by the brown crosses) have much

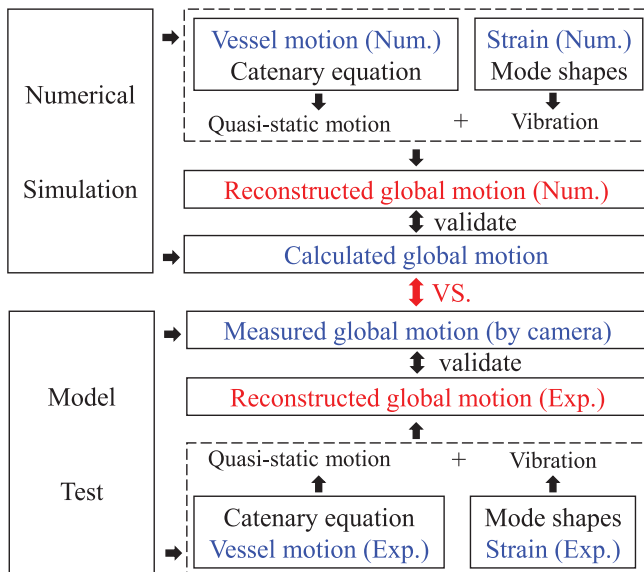


Figure 5. Numerical and experimental validation and comparison chart (Num. stands for numerical, Exp. stands for experimental). This figure is available in colour online.

Table 2. Selected cases for analysis.

| Case No. | Case name   | $A_{im}$ (m) | $A_i$ (m) | $T_{im}$ (s) | $T_i$ (s) |
|----------|-------------|--------------|-----------|--------------|-----------|
| 1        | H_A0105T596 | 0.105        | 2         | 5.96         | 26        |
| 2        | H_A021T481  | 0.21         | 4         | 4.81         | 21        |
| 3        | H_A037T504  | 0.37         | 7.05      | 5.04         | 22        |

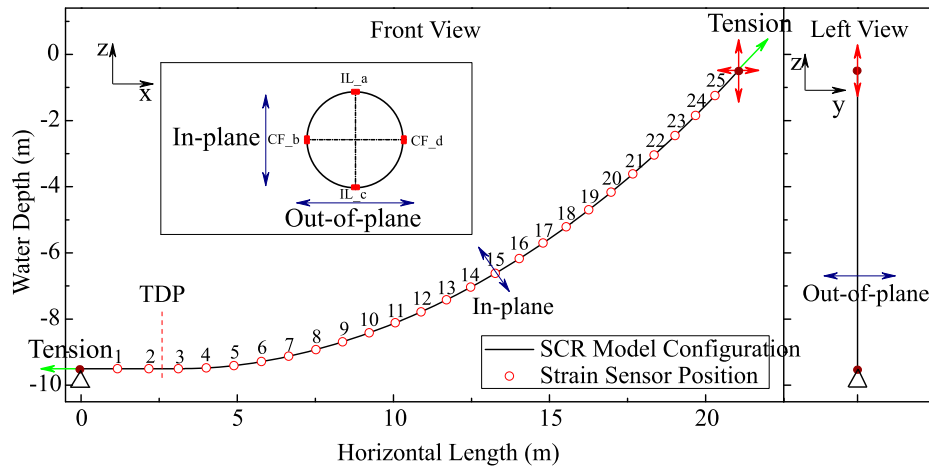


Figure 6. Truncated SCR model configuration and strain sensor locations. This figure is available in colour online.

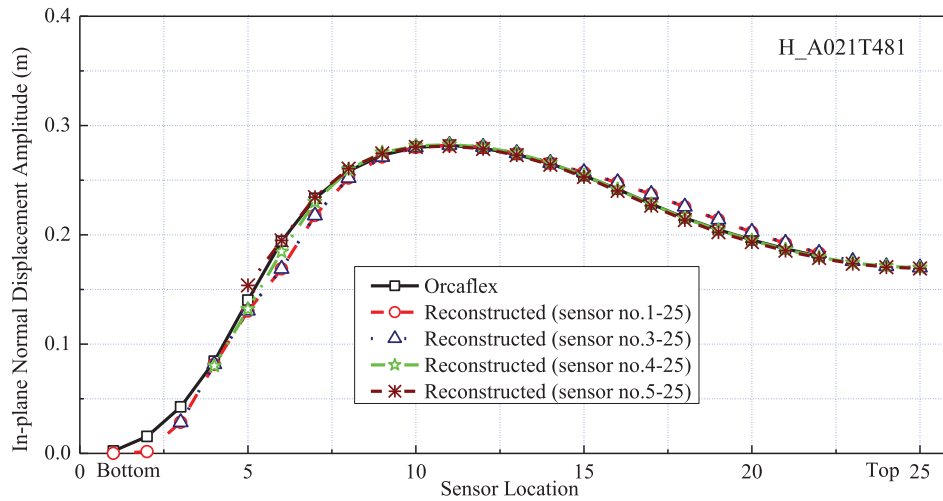


Figure 7. Reconstructed in-plane normal displacement amplitude comparison by using different sensor locations (case H\_A021T481). This figure is available in colour online.

better agreements with the Orcaflex calculations. It is the same observation for the other two selected cases. Therefore, we conclude that we have to abandon the flow line and TDP regions for the motion reconstruction. The initial sensor location considered in the motion reconstruction is sensor location 4 for our model.

It should be mentioned that the priority of the motion reconstruction methodology proposed in this paper is firstly to capture the maximum displacement/velocity amplitude and the corresponding locations, because these are the places where the maximum hydrodynamic forces are expected, and these locations are also typically associated with the ‘power-in’ region for the VIV responses. Secondly, the overall agreement between the reconstructed and the real motions is also quite important in the future identification of the hydrodynamic coefficients distribution. To the SCR under vessel motion, the riser motion around the TDP region is also extremely important since highly non-linear problems centralise in this

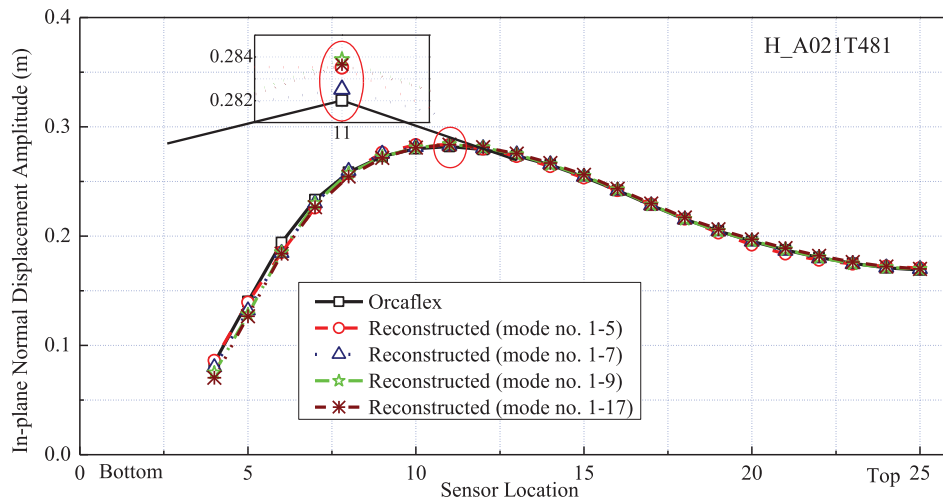
location including the TDP variation, riser-soil interaction and trenching. We have to admit that the local motion around the TDP region cannot be well captured in this paper. Further targeted reconstruction method should be developed for this particular problem separately.

### 5.1.2. Mode number effect

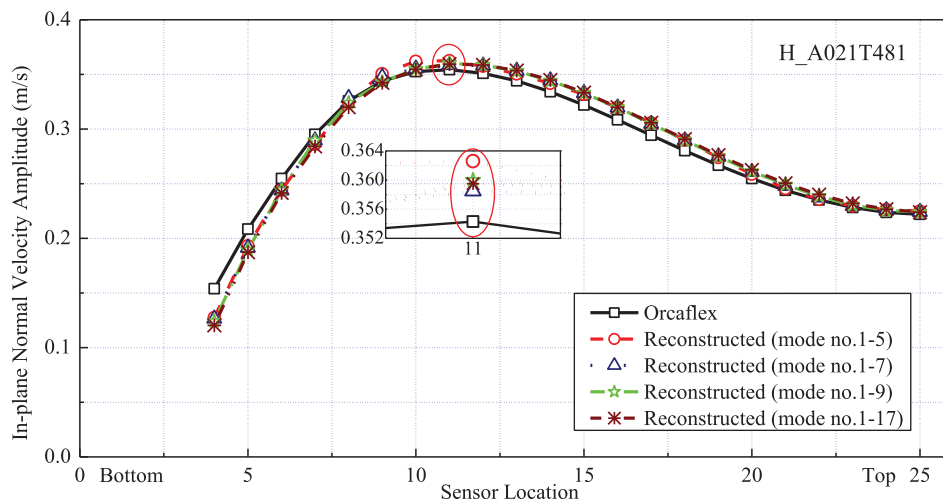
Figure 8 presents the comparison on the in-plane normal displacement amplitude among the conditions using different mode number combinations for the case H\_A021T481. It can be seen that all the four reconstruction results agree quite well with the directly calculated displacement by Orcaflex. But the best approximation is the second group using mode number from 1 to 7 as indicated by the navy triangles, shown in the enlarged window in Figure 8.

Figure 9 presents the comparison on the in-plane normal velocity amplitude among the conditions using different mode number combinations for the case H\_A021T481.





**Figure 8.** Reconstructed in-plane normal displacement amplitude comparison by using different number of modes (case H\_A021T481). This figure is available in colour online.



**Figure 9.** Reconstructed in-plane normal velocity amplitude comparison by using different number of modes (case H\_A021T481). This figure is available in colour online.

Although all the four groups have underestimated the riser motion velocity at the lower sag-bend region before the maximum motion velocity location and have overestimated the motion velocity at the upper sag-bend region, the same conclusion can be drawn where the second group is the best in reconstructing the motion velocity, and the error at the maximum velocity location is quite small at around 1.18%.

Based on the above sensor location and mode number analysis, we have concluded that by using sensor location from 4 to 25 and mode number 1–7 gives the best approximation to the real riser motion for the case H\_A021T481. Figures 10–13 present the reconstructed motion by using such parameters in different aspects, comparing to the real riser motion.

Figures 10 and 11 are the in-plane normal displacement and velocity amplitude comparisons between the calculation and reconstruction, respectively, which were also mentioned in Figures 8 and 9. They are plotted here again for better illustration of the reconstruction results.

Figure 12 presents the comparison of the reconstructed and directly calculated displacement time history at the maximum displacement location, sensor location 11. The subplot Figure 12(a) shows the vessel motion time histories for reference. The subplot Figure 12(b) evidently demonstrates the perfect fit of the reconstruction motion displacement (black solid line) compared to calculation (red dashed line) with the time evolution. The quasi-static motion (navy dot line) and dynamic vibration (green dot-dashed line) components are also presented in Figure 12(b), which reveals their contributions to the total motion. The comparison indicates that the quasi-static motion is the dominant contributor at sensor location 11, different contribution rate may apply at different locations. But we should keep in mind that the overall agreement between the reconstructed and directly calculated motion depends on the accurate reconstruction on both quasi-static and dynamic motion.

Figure 13 further illustrates the comparison between the calculated (left in Figure 13) and reconstructed (right in Figure 13)

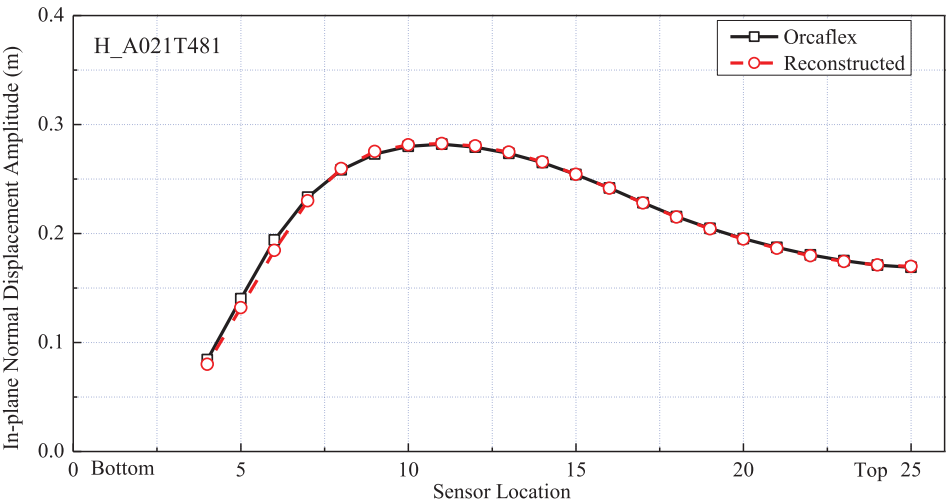


Figure 10. Reconstructed in-plane normal displacement amplitude comparison (case H\_A021T481). This figure is available in colour online.

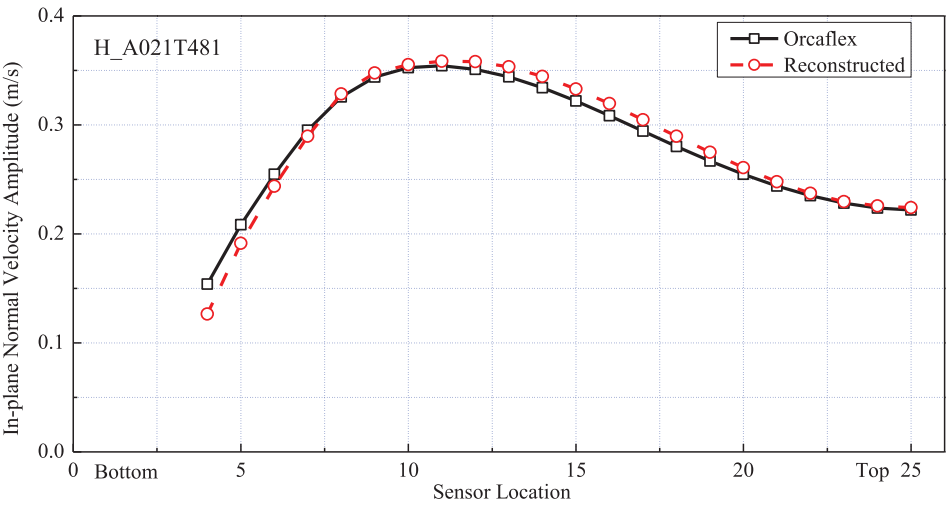


Figure 11. Reconstructed in-plane normal velocity amplitude comparison (case H\_A021T481). This figure is available in colour online.

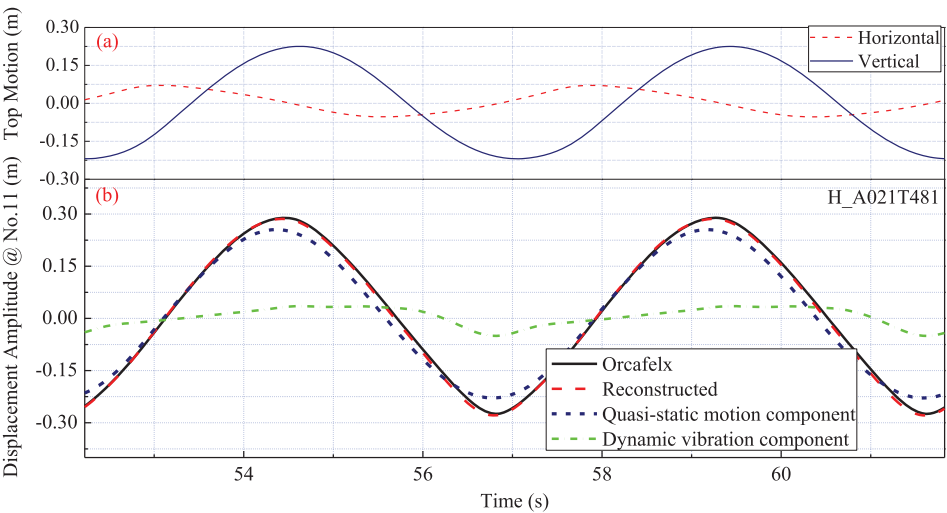


Figure 12. Reconstructed in-plane normal displacement time history comparison at sensor location 11 (case H\_A021T481) (row a: top vessel motion time histories; row b: normal displacement time history comparison at sensor location 11). This figure is available in colour online.

riser motion velocity distribution in contour plots. For both figures, the subplot 'a' presents the horizontal and vertical vessel motion displacement time histories, subplot 'b' is the contour plot which presents the riser in-plane normal motion velocity along the riser and with the time evolvement. Both contour plots are using the same colour map from 0 to 0.35 m/s, therefore, it is quite straightforward to reflect the velocity deviation by the colour difference.

Through the comparison, the reconstructed velocity agrees sufficiently well with the real velocity distribution both in time and along the entire riser span. The minor visible difference locates at the bottom region of the riser when the vessel reaches its trough location, for example, when time = 56–57 s. With such overall comparison in Figure 13, we can conclude that the motion reconstruction method successfully represents the global riser motion under vessel.

Since we have mentioned that the top priority of this reconstruction method is to find out the maximum motion amplitudes and the associated locations, therefore, the

reconstruction error for the displacement and velocity amplitude at each sensor location is defined as

$$\xi_A(s) = \frac{|A_{re}(s) - A_{orca}(s)|}{\max(A_{orca}(s))}$$

$$\xi_V(s) = \frac{|V_{re}(s) - V_{orca}(s)|}{\max(V_{orca}(s))} \quad (8)$$

where  $A_{re}(s)$ ,  $V_{re}(s)$  are the reconstructed displacement and velocity amplitudes at given axial location  $s$ ,  $A_{orca}(s)$ ,  $V_{orca}(s)$  are the calculated displacement and velocity amplitudes by Orcaflex.  $\xi_A(s)$ ,  $\xi_V(s)$  are the relative reconstruction errors at different sensor locations.

Figure 14 presents the error distribution along the riser for both displacement and velocity by using sensor location from 4 to 25 and mode number from 1 to 7 for the case H\_A021T481. By comparison, the error of the velocity is larger than the error of the displacement. Most of the velocity errors are within 3% and the displacement errors are within 1%.

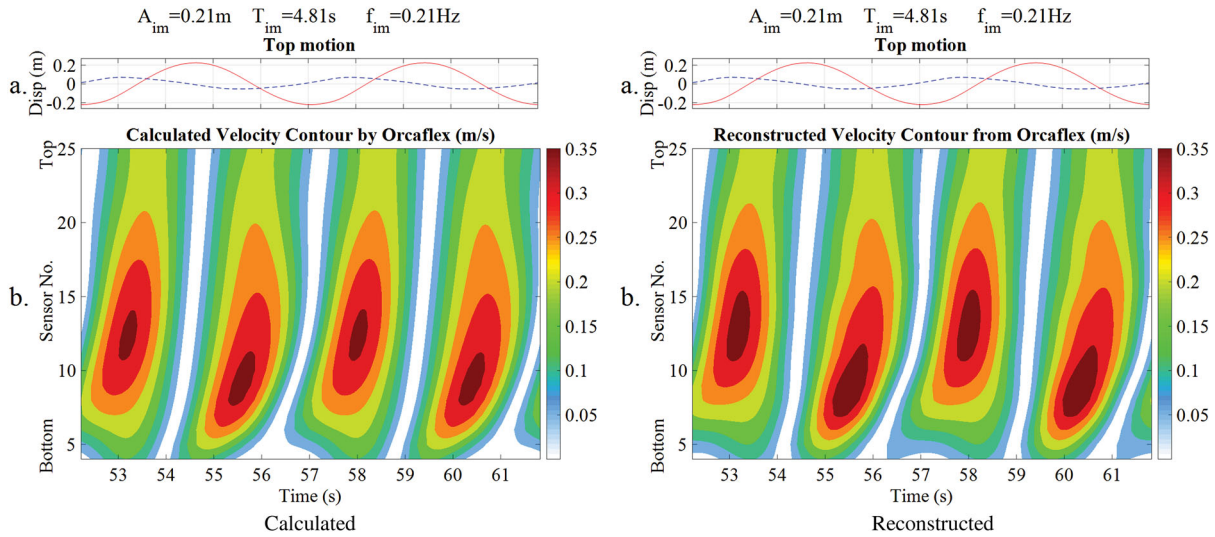


Figure 13. Calculated and reconstructed velocity contour comparison (case H\_A021T481) (in each figure, row a: top vessel motion time histories; row b: normal velocity contour plot). This figure is available in colour online.

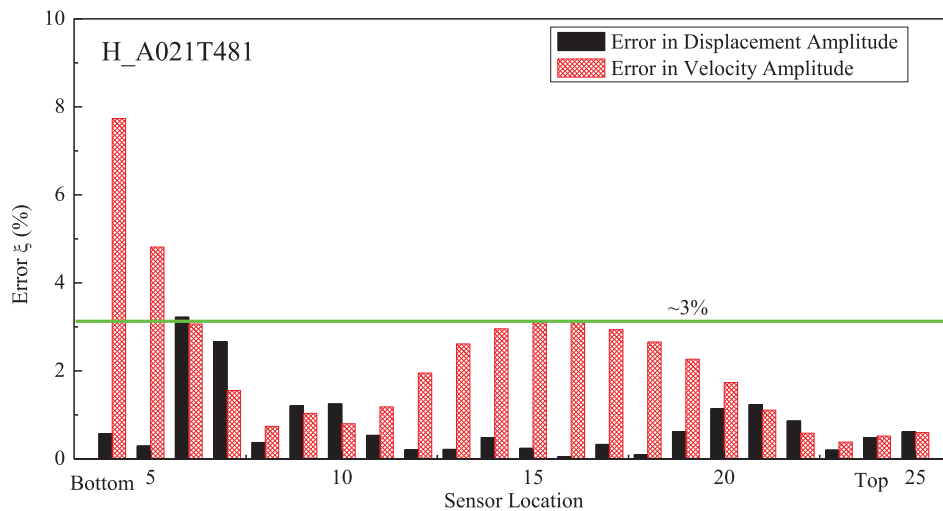


Figure 14. Reconstructed displacement and velocity error distribution along the riser (case H\_A021T481). This figure is available in colour online.

largest error for the velocity occurs at the lowest location near the TDP, this is as expected, partly due to the highly non-linear effect we have mentioned above. Generally speaking, the error of the proposed reconstruction method is within a satisfactory level.

The similar procedure is also performed for the other two cases, where mode number 1–5 is suggested for the case H\_A0105T596 and mode number 1–11 is suggested for the case H\_A037T504. For the purpose of simplicity, the detailed comparison results for the other two cases are not presented here, but the error information is summarised in Table 3 for reference. It can be summarised from Table 3 that the maximum reconstruction error has an increasing trend when the vessel motion gets tougher, especially a large velocity error up to 18.34% is observed for the case H\_A037T504. However, it's worth mentioning that H\_A037T504 is the case where the prototype vessel heave motion amplitude is significantly large, up to 7 m, which would lead to a larger TDP variation. Such case with an enormous heave amplitude is definitely with a very small probability of occurrence in the practical offshore application. What's more, the large errors are all at the lowest sensor location near the TDP. Nevertheless, the corresponding errors at the maximum displacement and maximum velocity locations are all maintained in a satisfactory level near or within 1%.

**Table 3.** Summarised results for all the three cases.

| Case No.                   | 1                   | 2                   | 3                   |
|----------------------------|---------------------|---------------------|---------------------|
| Case name                  | H_A0105T596         | H_A021T481          | H_A037T504          |
| Sensor location            | 4-25                | 4-25                | 4-25                |
| Mode number                | 1-5                 | 1-7                 | 1-11                |
| $\xi_{A\_max\_A}$          | 0.60%               | 0.18%               | 0.61%               |
| Max ( $\xi_A(s)$ )         | 1.67%               | 3.45%               | 6.61%               |
| $\mu \pm \sigma(\xi_A(s))$ | $0.77\% \pm 0.48\%$ | $0.63\% \pm 0.92\%$ | $1.79\% \pm 1.77\%$ |
| $\xi_{V\_max\_V}$          | 0.10%               | 1.18%               | 0.83%               |
| Max ( $\xi_V(s)$ )         | 1.39%               | 7.74%               | 18.34%              |
| $\mu \pm \sigma(\xi_V(s))$ | $0.61\% \pm 0.44\%$ | $2.16\% \pm 1.70\%$ | $3.78\% \pm 3.99\%$ |

Note:  $\xi_{A\_max\_A}$ ,  $\xi_{V\_max\_V}$  are the displacement and velocity error at the maximum displacement and maximum velocity location; Max,  $\mu$  and  $\sigma$  represent the maximum, mean and standard deviation of the error based on the results at all the sensor locations.

### 5.1.3. Noise effect

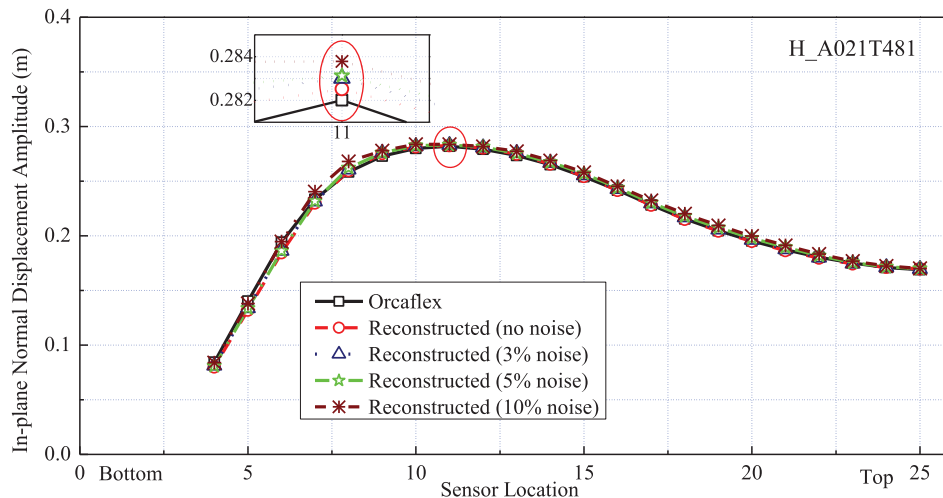
As has been mentioned that the ultimate goal for the proposed motion reconstruction method is to obtain the riser motion based on the experimental or field measurements. In such cases, errors in the measurements are always inevitable. Therefore, an uncertainty analysis considering different kinds of noise level in the measurements is carried out to evaluate the robustness of the proposed reconstruction methodology. In this paper, only the errors in the strain measurements are considered. They are realised by introducing the white noise into the total dynamic strain time histories at all the measuring stations. The noise level is defined by

$$\Delta \varepsilon(s) = \frac{\sigma(\varepsilon_{err}(t, s))}{\sigma(\varepsilon_{dyn\_orca}(t, s))} \quad (9)$$

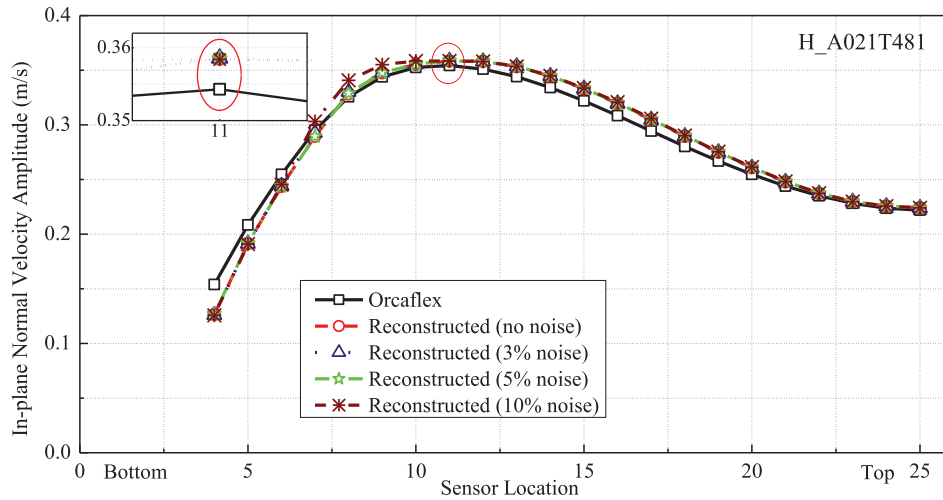
where  $\sigma(\varepsilon_{err}(t, s))$  is the standard deviation of the strain noise time history at axial length  $s$ ,  $\sigma(\varepsilon_{dyn\_orca}(t, s))$  is the standard deviation of the dynamic strain time history calculated by Orcaflex,  $\varepsilon_{dyn\_orca}(t, s)$  contains dynamic strain from both quasi-static motion and dynamic vibration.  $\Delta \varepsilon$  is the noise level we defined, and three different kinds of noise level are evaluated in this paper. They are 3%, 5% and 10%.

Figure 15 presents the reconstructed in-plane normal displacement amplitude distribution under different noise level, compared to the directly calculated motion. It can be surprisingly found that all the four reconstructed motion displacements fit well with the original motion displacement, although there is a subtle increasing deviation with increasing noises level, as shown by the enlarged window in Figure 15. Figure 16 shows the corresponding velocity comparison, from which similar conclusion can be drawn that the reconstructed velocity agrees well with the true velocity under different noise level.

Table 4 summarises the reconstruction error of the displacement and velocity under different noise level. It can be seen that all the error parameters in Table 4 stay within an acceptable range. This indicates the good tolerance of the proposed motion reconstruction method in measurements with different noise level.



**Figure 15.** Reconstructed in-plane normal displacement amplitude comparison considering different noise level (case H\_A021T481). This figure is available in colour online.



**Figure 16.** Reconstructed in-plane normal velocity amplitude comparison considering different noise level (case H\_A021T481). This figure is available in colour online.

**Table 4.** Reconstruction error under different noise level for H\_A021T481.

| Noise level                | 0                 | 3%                | 5%                | 10%               |
|----------------------------|-------------------|-------------------|-------------------|-------------------|
| $\xi_{A\_max\_A}$          | 0.18%             | 0.37%             | 0.25%             | 0.48%             |
| Max ( $\xi_A(s)$ )         | 3.45%             | 3.09%             | 2.23%             | 2.29%             |
| $\mu \pm \sigma(\xi_A(s))$ | 0.63% $\pm$ 0.92% | 0.70% $\pm$ 0.77% | 0.69% $\pm$ 0.60% | 1.41% $\pm$ 0.61% |
| $\xi_{V\_max\_V}$          | 1.18%             | 1.20%             | 1.18%             | 1.34%             |
| Max ( $\xi_V(s)$ )         | 7.74%             | 7.78%             | 7.80%             | 7.29%             |
| $\mu \pm \sigma(\xi_V(s))$ | 2.16% $\pm$ 1.70% | 2.15% $\pm$ 1.71% | 2.20% $\pm$ 1.72% | 2.19% $\pm$ 1.62% |

Note:  $\xi_{A\_max\_A}$ ,  $\xi_{V\_max\_V}$  are the displacement and velocity error at the maximum displacement and maximum velocity location; Max,  $\mu$  and  $\sigma$  represent the maximum, mean and standard deviation of the error based on the results at all the sensor locations.

In summary, this section gives a very detailed numerical validation on the proposed motion reconstruction method. The numerical simulations are very effective since both the ‘knowns’ and ‘unknowns’ in the reconstruction method are

available. Considering that the motion reconstruction we proposed is a general method which is supposed to be applied for other slender structures subjected to dynamic load and dynamic boundary conditions as well. It is recommended that the abovementioned numerical validation should always be carried out before its application on practical experimental or field measurements.

## 5.2. Experimental validation results

As has been mentioned that there was one underwater camera installed to measure the riser in-plane motion under vessel motion near sensor location 13. Based on the video footages, we have picked two representative frames during one vessel motion period for each test case: one when the riser segment reaches its uppermost end and the other one at its lowermost end. By blending the two frames, as demonstrated in Figure 17

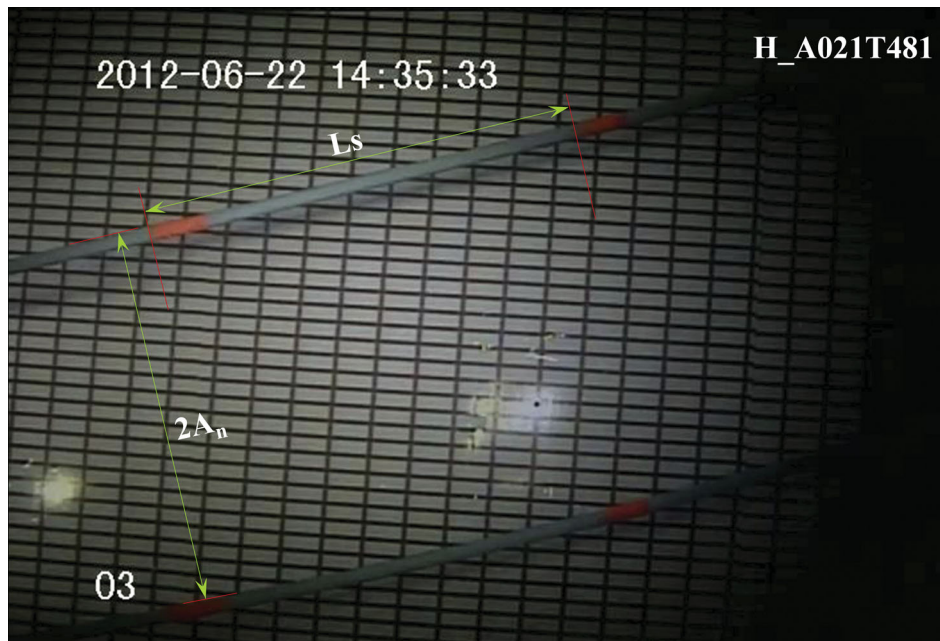


**Figure 17.** Riser in-plane motion validation based on underwater camera video frames (case H\_A021T481). This figure is available in colour online.



for the case H\_A021T481, we can easily calculate the displacement amplitude  $A_n$  of the riser in-plane motion at sensor location 13 based on the length relationship of the two lines between the green arrows, considering the length of  $L_s$  is known beforehand.

By adopting the numerically validated motion reconstruction method, the riser in-plane global motion during the model test is reconstructed and then compared to the Orcaflex calculated results, as shown in Figure 18. The displacement amplitude at sensor location 13 for the case H\_A021T481 based on underwater camera measurements in Figure 17 is also added for the purpose of experimental validation, as shown by the red pentagon. Similar experimental validations for the other two cases are also presented in Figures 19 and 20. The comparisons in these three figures convey two straightforward information: (1) the motion reconstruction method is experimentally validated and shows good accuracy; (2) there is a noticeable difference between the numerically calculated and experimentally measured riser in-plane global motion. The numerical results underestimate the motion at the lower sag-bend but overestimate the motion at the upper sag-bend. The deviation is especially evitable for the small vessel motion

case. This motion deviation is supposed to be caused by the inadequate understanding on the real hydrodynamic load distribution.

### 5.3. Hydrodynamic coefficients of a SCR under vessel motion

Considering the fact that the real riser motion in the model test is quite different from the numerical results, as shown in Figures 18–20. This is partly because of the drag amplification caused by the existence of VIV (Huang et al. 2011). As has been pointed out, the most straight forward way is to obtain the true hydrodynamic coefficients distribution by inversed analysis. This will be a promising future work due to the complexity of the theory and methodology. This section is, however, using a trial and error method to demonstrate the drag amplification effect during the model test.

Generally speaking, we have performed numerical cases using different drag coefficients, but maintain the added mass coefficient to be constant at 1. Figure 21 presents the displacement comparison using different drag coefficient for the case H\_A021T481 as an example. It can be seen that by increasing

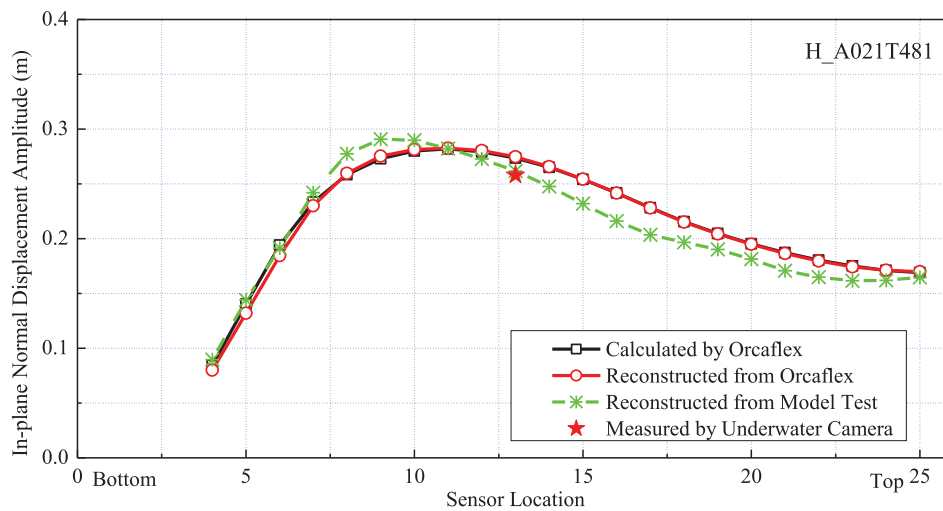


Figure 18. Reconstructed in-plane normal displacement amplitude based on experimental measurements (case H\_A021T481). This figure is available in colour online.

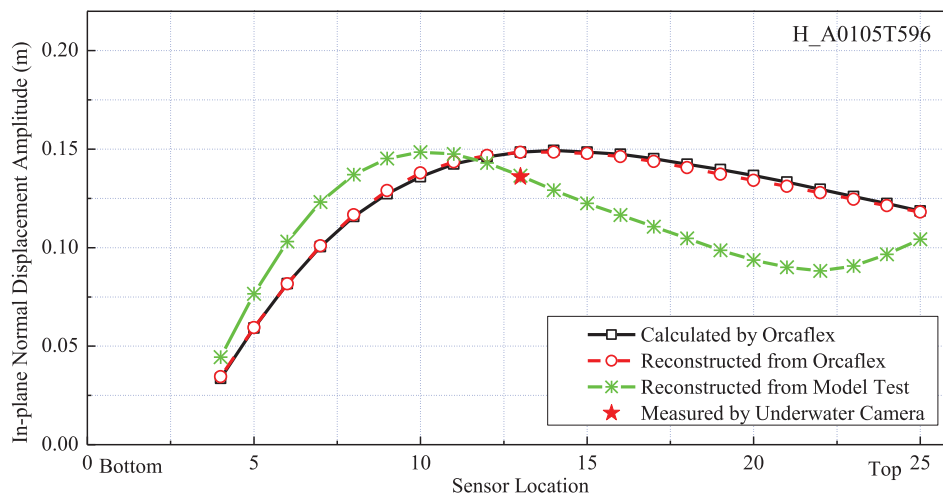


Figure 19. Reconstructed in-plane normal displacement amplitude based on experimental measurements (case H\_A0105T596). This figure is available in colour online.

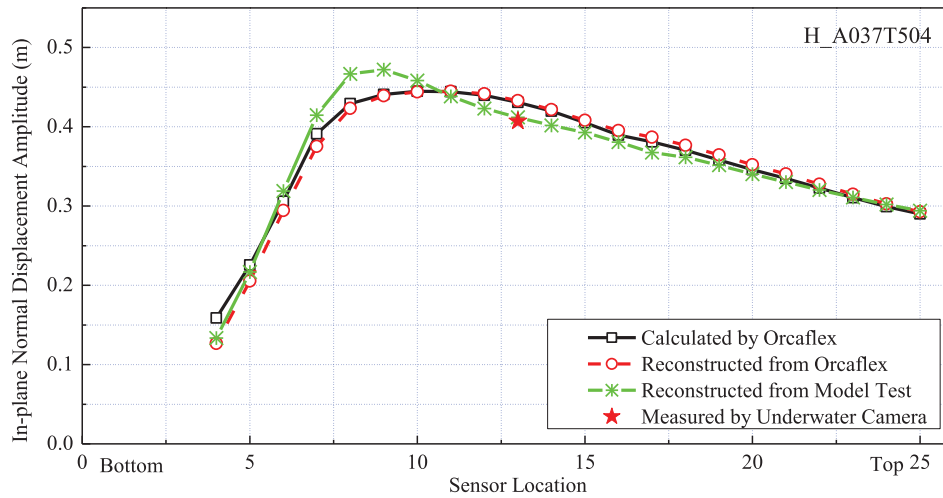


Figure 20. Reconstructed in-plane normal displacement amplitude based on experimental measurements (case H\_A037T504). This figure is available in colour online.

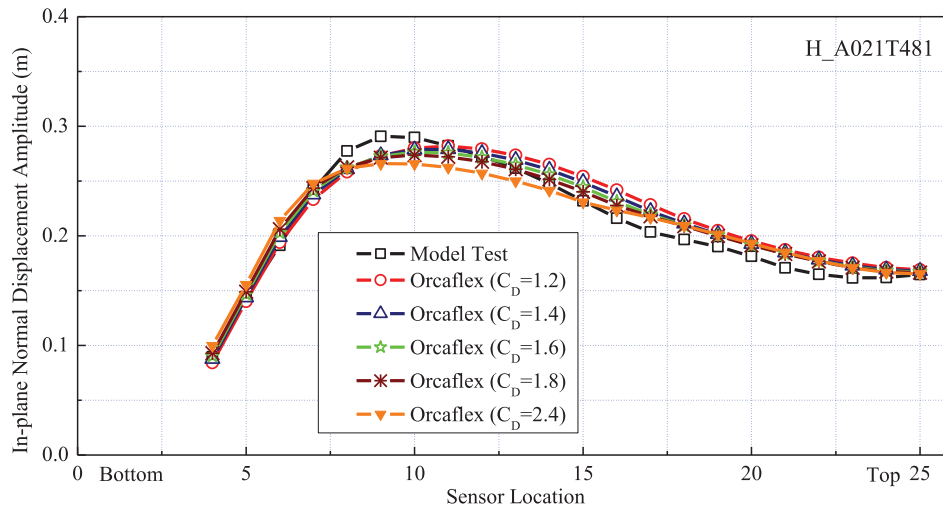


Figure 21. In-plane normal displacement amplitude comparison considering different drag coefficient (case H\_A021T481). This figure is available in colour online.

the drag coefficient, the riser motion at the upper sag-bend is suppressed and approximating the experimental measurements, but the motion near the lower sag-bend is slightly increased and we are not able to represent the maximum displacement observed from the model test. In another word, none of the numerical results fit quite well with the experimental measurements.

We further tried a more complicated way by defining different drag coefficient at different riser regions. Figure 22 illustrates the results from the case in which three drag coefficients: 1.3, 1.6 and 1.9 are, respectively, defined for three different regions, each with equal axial length from the bottom to the top of the riser. The numerical results by using conventional drag coefficient of 1.2 and experimental measurements are also presented in Figure 22 for comparison. It should be mentioned that the combination of different drag coefficient using 1.3, 1.6 and 1.9 is the best approximation against the experimental results out of ten attempts using other combinations we have tried. Although there is still some deviation between the experimental and the numerical results using suggested drag coefficients, it's already far better than the case assuming  $C_D = 1.2$ . It is expected that

the real hydrodynamic load distribution will be different and more scattered in values along the riser span than the three coefficients combination we present here. Nevertheless, the comparison in Figure 22 emphasises the significant contribution of the drag amplification on the riser global responses under vessel motion. This drag amplification is most probably caused by out-of-plane VIV, where a larger drag occurs because the current 'sees' a larger projected area due to the riser out-of-plane vibration.

## 6. Conclusion

This paper proposed a generalised global motion reconstruction method for the marine slender structures characterised with large displacement but small deformation, assuming the riser global motion can be divided into quasi-static motion and dynamic vibration. The proposed methodology is validated both numerically and experimentally with satisfactory accuracy. The reconstruction error for the maximum displacement and velocity is maintained in a satisfactory level near or within 1%. Meanwhile, parameters like sensor location and mode number to be used in the motion reconstruction are also optimised and

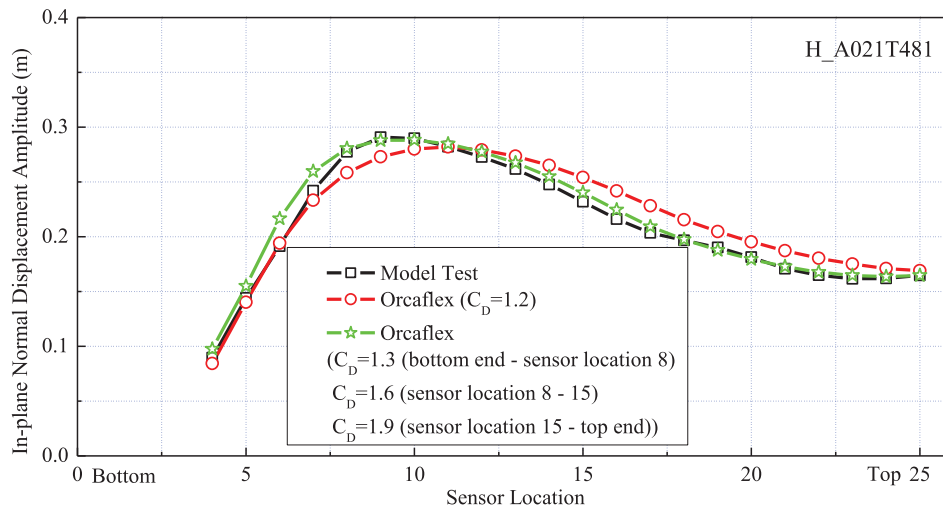


**Figure 22.** In-plane normal displacement amplitude comparison considering different drag coefficient along the riser (case H\_A021T481). This figure is available in colour online.

recommended. Uncertainty analysis considering measurements with different artificial noise level further indicates the proposed methods is quite robust in handling the measurements with different noise level. Most importantly, comparison between the measured and numerical simulation results suggests that there is a significant drag amplification due to the existence of the vessel motion-induced VIV. Further studies are recommended to identify the real hydrodynamic force coefficients distribution along the SCR considering the VIV effects.

Generally speaking, the proposed motion reconstruction methodology successfully captures the riser in-plane global motion under vessel motion, which provides essential inputs for the future research on accurate hydrodynamic load distribution. Hopefully, this method will be useful for gaining a better understanding on VIV induced by vessel motion, and for the development of future prediction models.

## Acknowledgements

The authors would particularly like to thank Statoil for the permission to use these data for this publication.

## Disclosure statement

No potential conflict of interest was reported by the author(s).

## Funding

The authors gratefully acknowledge the financial support from Statoil, Norway, for the research program: VIV effects in sag-bends of SCRs. Support from the National Science Foundation of China [grant number 51279101], [grant number 51490674] and China Scholarship Council are also greatly appreciated.

## ORCID

Jungao Wang  <http://orcid.org/0000-0003-3024-2951>

## References

- DNV. 2001. OS-F201: dynamic risers. Hovik: DNV Services, Research and Publications.
- DNV. 2005. RP-C203: fatigue design of offshore steel structures. Hovik: Det Norske Veritas.
- DNV. 2010. RP-F205: global performance analysis of deepwater floating structures. Hovik: Det Norske Veritas.
- Faltinsen O. 1993. Sea loads on ships and offshore structures. Cambridge: Cambridge University Press.
- Gopalkrishnan R. 1993. Vortex-induced forces on oscillating bluff cylinders (No. WHOI-92-38). Falmouth: Woods Hole Oceanographic Institution.
- Grant RG, Litton RW, Mamidipudi P. 1999. Highly compliant rigid (HCR) riser model tests and analysis. Proceedings of the Offshore Technology Conference, Huston, Paper No: OTC-10973-MS.
- Huang S, Khorasanchi M, Herfjord K. 2011. Drag amplification of long flexible riser models undergoing multi-mode VIV in uniform currents. *J Fluids Struct.* 27:342–353.
- Larsen CM, Vikestad K, Yttervik R, Passano E, Baarholm GS. 2001. VIVANA theory manual. Trondheim: Marintek.
- Mekha BB. 2001. New frontiers in the design of steel catenary risers for floating production systems. *J Offshore Mech Arctic Eng.* 123:153–158.
- Orcina. 2012. OrcaFlex manual: version 9.5d. Daltongate, UK.
- Song L, Fu S, Cao J, Ma L, Wu J. 2016. An investigation into the hydrodynamics of a flexible riser undergoing vortex-induced vibration. *J Fluids Struct.* 63:325–350.
- Sumer BM. 2006. Hydrodynamics around cylindrical structures. Singapore: World Scientific Publishing.
- Vandiver JK, Li L. 2005. Shear7 V4. 4 program theoretical manual. Cambridge: Department of Ocean Engineering, Massachusetts Institute of Technology.
- Wang J, Fu S, Baarholm R. 2014. Vortex-induced vibration of steel catenary riser under vessel motion. Proceedings of the 33rd OMAE, San Francisco. Paper No. OMAE2014-23584.
- Wang J, Fu S, Baarholm R, Wu J, Larsen CM. 2014. Fatigue damage of a steel catenary riser from vortex-induced vibration caused by vessel motions. *Mar Struct.* 39:131–156.
- Wang J, Fu S, Baarholm R, Wu J, Larsen CM. 2015. Out-of-plane vortex-induced vibration of a steel catenary riser caused by vessel motions. *Ocean Eng.* 109:389–400.
- Wang J, Fu S, Larsen CM, Baarholm R, Wu J, Lie H. 2017. Dominant parameters for vortex-induced vibration of a steel catenary riser under vessel motion. *Ocean Eng.* 136:260–271.
- Wu J. 2011. Hydrodynamic force identification from stochastic vortex induced vibration experiments with slender beams. Trondheim: Norwegian University of Science and Technology.